A Wireless Image Sensor for Real-Time, In Vivo Fluorescence Microscopy in Cancer Therapy

Rozhan Rabbani
Mekhail Anwar, Ed.
Vladimir Stojanovic, Ed.

Electrical Engineering and Computer Sciences
University of California, Berkeley

May 1, 2024

Acknowledgement

A Wireless Image Sensor for Real-Time, *In Vivo* Fluorescence Microscopy in Cancer
Therapy

by

Rozhan Rabbani

A dissertation submitted in partial satisfaction of the

requirements for the degree of

Master

in

Electrical Engineering and Computer Sciences

in the

Graduate Division

of the

University of California, Berkeley

Committee in charge:
Professor Mekhail Anwar
Professor Vladimir Stojanovic

Spring 2023

A Wireless Image Sensor for Real-Time, *In Vivo* Fluorescence Microscopy in Cancer Therapy

A Wireless Image Sensor for Real-Time, *In Vivo* Fluorescence Microscopy in Cancer Therapy
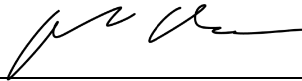
by Rozhan Rabbani

Research Project

Submitted to the Department of Electrical Engineering and Computer Sciences, University of California at Berkeley, in partial satisfaction of the requirements for the degree of **Master of Science, Plan II**.

Approval for the Report and Comprehensive Examination:

Committee:

Professor Mekhail Anwar
Research Advisor

05/09/2023

(Date)

* * * * * * *

Professor Vladimir Stojanovic
Second Reader

5/9/2023

(Date)

Abstract

A Wireless Image Sensor for Real-Time, *In Vivo* Fluorescence Microscopy in Cancer Therapy
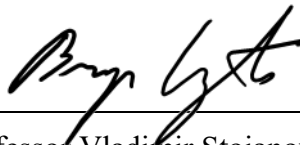
by

Rozhan Rabbani

Master in Electrical Engineering and Computer Sciences

University of California, Berkeley

,

Millimeter-scale, implantable wireless sensors enable unprecedented access to *in vivo* information, providing insights for diagnosis and treatment guidance across numerous medical conditions, including cancer therapy. For instance, one of the high impact therapeutics where access to cellular-level information from deep inside the body in real-time is critical is Immunotherapy. This information can be utilized in improving the efficacy of the treatment leading to higher response rates for patients. However, current imaging modalities suffer from inadequate resolution and lack of compatibility needed to monitor the tissue and the immune response continuously. Therefore, there's a need for a miniaturized image sensor to monitor the biological processes dynamically. To address these challenges, we propose a mm-sized, ultrasonically powered, wireless, lensless CMOS image sensor for real-time fluorescence microscopy from within tissue. The proposed device eliminates the need for bulky optics such as lenses or bulky electronics such as batteries and external wiring. The design incorporates a 36×40-pixel CMOS image sensor with power harvesting interface measuring only $2.4 \times 4.7mm^2$, a sub-mm-sized laser diode (LD), a single piezoceramic and a storage capacitor. The piezoceramic harvests energy from the acoustic waves to power up the sensor and transfer data back to an external receiver via ultrasound. The overall system exhibits detection of $140\mu m$ features on a United States Air Force (USAF) resolution test target opening the door to continual *in vivo* monitoring of microscopic cell foci and increasing visibility into the tumor microenvironment. Future work to further decrease the size of this proposed untethered device will enable minimally invasive implantation of the device using a biopsy needle eliminating the need for surgeries and facilitating its use for Immunotherapy patients.

Acknowledgments

I would like to express my gratitude to my advisor, Professor Mekhail Anwar, for his guidance and support throughout the project. Thanks to his insights, I had the incredible opportunity to work on a project that has the potential to impact healthcare positively. I am also grateful to Professor Vladimir Stojanovic for co-advising me and providing me with generous assistance during the project, as well as to Professor Rikky Muller for her collaboration and guidance.

I would like to extend my sincere appreciation to my colleagues, Chris Najafiaghdam, Efthymios Philip Papageorgiou, Mohammad Meraj Ghanbari and Micah Roschelle and all the members of Anwarlab for their unwavering help and support throughout the project.

Next, I would like to express my heartfelt thanks to my dear friends, Behrooz Ghorbani, Mahsa Sadeghi, Rebekah Zhao, Alisha Menon, Sorour Tarighi and Zohreh Azizi for their sincere support during my studies.

Finally, I want to express my deepest gratitude to my beloved family and my wonderful sister, Baran, whose constant support has meant everything to me. I miss them more than words can say.

Contents

List of Figures

Chapter 1

Introduction

1.1   Motivation

Miniaturized wireless implantable sensors enable unprecedented access to *in vivo* information, guiding diagnosis and treatment across numerous medical conditions, based on real-time feedback from the patient's own tissue [1],[2]. Using this information could lead to quickly adjusting therapy, which would address a critical challenge in medicine: the significant variation in patient response to therapy, and the absence of any means to observe the real-time, multicellular response to treatment in tissue [3].

Monitoring deep inside the body with sufficient resolution to see real-time changes is critical for understanding the dynamics of biological processes. In cancer therapy, obtaining access to *in vivo* imaging information is crucial, particularly in Immunotherapy, a game changing therapeutic which stimulates the patient's immune system to target and eliminate cancerous cells [4]. There are several Immunotherapy drugs that work in different ways. Immune checkpoint inhibitors block the immune system checkpoints which prevent the immune system's response to cancer. CAR T-cell therapy works by removing some T-cells, a type of the immune cells, from the blood. Once the T-cells are engineered to express these receptors to cancer cells, they are injected back to the body to destroy cancer. Some treatments include using Cytokines which are small proteins that carry messages between cells in order to stimulate the immune system to attack cancer. A cancer vaccine can also trigger the immune system to recognize and fight cancer. Although multiple clinical trials have indicated an increase in overall survival with immunotherapy [5], [6], less than 20-30% of the overall patients respond to the treatment [7]. Furthermore, the therapy carries risks such as autoimmune side effects and imposes financial costs [8]. In addition, the possibility of losing the chance for a cure due to time spent on ineffective therapy underscores the importance of quickly identifying non-responders and modifying therapy based on an early response evaluation, which can help personalize the treatment for each patient and increase its efficacy. Intratumoral imaging at the cellular level is vital for identifying early responders and non-responders, as well as for gaining insight into the mechanisms of treatment resis-

tance [9]. This information can be leveraged to personalize the treatment for each patient, transforming a non-responsive tumor into a responsive one.

1.2   Challenges

There are several critical requirements that must be addressed for an imaging system to be effectively applicable for monitoring the immune response in immunotherapy. First, the imaging system is required to image cellular changes at the earliest possible time point. Any delay leads to prolonging the therapy and lowering the chances of cure. Additionally, since the immune response is a complex feedback network among many cell types, including cells acting as positive regulators and others in negative feedback [10], the imaging modalities must be capable of multiplexed imaging. Additionally, the distribution profile of the cells involved in the immune system and their relationship to each other spatially is key to assessing response imposing requirements for the spatial resolution of the imaging system. Patients exhibit different response "phenotypes" (defined as the physical distribution of immune cells within the tumor) [11]. To summarize, in order to study each patient's response over time relative to their initial baseline, an imaging system for cancer immunotherapy must meet several criteria. It should be millimeter-scale, wireless, capable of periodic imaging over days to months-long time scales and able to image multiple cell types and determine changes in their spatial arrangement from image to image. These factors can only be observed through microscopy of tissue biopsies, which is impractical due to the morbidity, cost, and logistics of repeated biopsies, especially when monitoring deep tissue sites.

Currently, biological response is evaluated with the existing clinical imaging modalities including computed tomography (CT), magnetic resonance imaging (MRI), positron emission tomography (PET), single-photon emission computed tomography (SPECT), ultrasound (US) and multimodal (CT/PET, PET/MRI, etc.) [12],[13]. Although MRI, PET and CT can image wide areas or the entire body, the clinical resolution of these platforms, defined as the change in tumor sufficient to be clinically meaningful, is often limited to centimeter-scale changes. Guidelines for immunotherapy such as iRECIST [14] mandate volumetric changes of 20% in the tumor size to confirm tumor growth, so even for a small tumor of $1-3cm$, this equates to a minimum of $0.2cm^3$. With the dimension of a cell being $\sim 10\mu m$, this equates to a minimum detectable change of 200 million cells, which can take months to manifest under these modalities.

Hence, the inability of modern clinical imaging tools to detect early response results in the loss of the opportunity for prompt therapeutic adaptation. Furthermore, the lack of molecular labeling in CT and MRI limits their capacity to monitor anything beyond anatomical changes, thereby restricting their resolution as discussed earlier. Although molecular-based PET and SPECT have been introduced for prostate and neuroendocrine cancers, they can only identify one type of tumor cells at a time, and their spatial resolution, limited to several millimeters at best, is still in the range of approximately 100 million cells due to the need to image through the body leading to scattering. Despite the ability to image at depth,

ultrasound imaging cannot detect microscopic changes due to its limited resolution of approximately $\sim 1mm$ and sensitivity to only anatomical changes [15], making it unsuitable for identifying the specific cell types required for assessing response. Traditional techniques without real-time monitoring are restricted to snapshots that are incapable of capturing the dynamics of key biological phenomena. Thus, a novel method for clinically imaging tumor response is required.

On the contrary, optical microscopy including fluorescence, confocal, bioluminescene, bright-field, phase contrast microscopy, etc., permits high-resolution, multiplexed imaging, which provides crucial information regarding the progression of diseases and the efficacy of treatments [16]. Fluorescence microscopy is a category of optical imaging that depends on small molecules that absorb light and emit light of a slightly longer wavelength ($\sim 50nm$) with lower energy. These molecules enable the visualization of biological entities by conjugating with cell or protein-specific antibodies and small molecules. For example, fluorescence microscopy with systematic injections of fluorescently-tagged cell-specific antibodies allows for 1) real-time monitoring with 2) cellular-level resolution of 3) multiple cell types simultaneously, which is not feasible with other imaging modalities. By changing the wavelength of the excitation light using appropriate optical filters such as multi-band pass filters to select emitted light, multiplexed imaging can be easily achieved without requiring additional changes to the imaging interface. Despite its advantages, optical microscopy is constrained by the limited depth of penetration of light transmitted from external optical sources, even with lower Near Infrared (NIR) wavelength absorption in the tissue [17]. Intravital microscopy (IVM) is an optical imaging modality that can leverage fluorescence to visualize *in vivo* processes using a surgically implanted window [18]. Although IVM offers high resolution, its visualization capabilities are restricted to depths of less than a few millimeters [15], limiting its use to tumors or organs at the tissue surface.

To enable high-resolution in-depth *in vivo* microscopy in patients, a platform must have a miniaturized light source and fluorescence imager, placed together deep inside the body. The imaging system also requires a wireless interface for power and data transfer to facilitate noninvasive real-time monitoring. Chronic wires extending out of the body pose an infection risk. Due to the inefficiency of fluorophores, a high-intensity optical source is necessary, typically on the order of $100mW/cm^2$ for microscope illuminations. Implantable light sources need to be laser diodes or LEDs for compactness. Laser diodes are preferable due to their single wavelength of illumination, as LEDs have a wider spectrum that can contribute significant background to fluorophore emission. However, supplying high power (10s of mW) and high currents ($10s\,of\,mA$) to enable adequate imaging time (10s to 100s of ms) presents challenges for the wireless system design. Supplying such a high instantaneous power source and communicating large amounts of data for each captured image imposes challenges on the design of the wireless system.

1.3 Previous Work

Recent works have introduced implantable sensors that exhibit power transfer and data communication for low-power applications up to several mW such as neural recording and stimulation, blood oxygenation sensing, pacemakers, etc. [19],[20],[21],[22]. However, wireless power transfer for System-on-Chips (SoCs) with high-power operations like optical excitation for fluorescence imaging has not been shown. Although state-of-the-art CMOS image sensors enable high-resolution fluorescence microscopy for various biomedical applications, they lack a wireless interface that would allow them to be used as untethered implantable sensors [23],[24],[25],[26]. Therefore, the proposed image sensors require large batteries or external wiring to transfer power and data and hence are not practical for chronic real-time *in vivo* monitoring. The fully wireless thermoacoustic image sensor introduced in [27] demonstrates fully wireless operation but does not provide the sensitivity and specificity needed to track cellular-level changes and components of the immune system dynamically. Fiber optic probes have shown *in vivo* imaging but their utility for continuous monitoring is limited by the invasiveness of the probe [28]. For data transfer, the wireless sensor is required to ensure robust communication for transmitting large amounts of image data per frame. High positional variations due to the inherent motion of the tissue in the body rule out analog communication despite its higher data rate as presented in [29]. Therefore, on-chip digitization of the sensor outputs to implement digital communication is needed.

1.4 System Overview

This thesis presents the design and implementation of a proof-of-concept mm-scale CMOS image sensor, capable of 1) on chip illumination 2) imaging with on-chip analog to digital conversion, and 3) wireless power and data transfer via ultrasound to address the challenges indicated above. An US link, as opposed to inductive coupling, optical and RF-based links [22], is chosen to leverage the low tissue attenuation ($\sim 0.5 dB/cm/MHz$) [30] and higher Food and Drug Administration (FDA) regulatory limit for power flux density ($720 mW/cm^2$ [31]) in the tissue. To allow for the high instantaneous power and currents needed for the laser diode operation, an off-chip storage capacitor stores wireless US energy to supply the system during intervals with high power consumption. To obviate the need for bulky optical lenses, a microfabricated angle-selective collimator is utilized to restrict the angle of incident light resulting in images with higher resolution and less blur building on the work presented in [32]. This imaging device powers up using wireless energy from the ultrasound link, and following commands encoded in the US transmissions, proceeds to illuminate using the attached laser diode while simultaneously capturing an image from fluorescently-labeled targets, and then serially converts each pixel to an 8-bit digital value and transmits data back to an external transducer via ultrasound backscattering. The system is capable of imaging a USAF test target with a resolution of $140 \mu m$ making the detection of microscopic cell foci plausible. In the future, the size of the eventual system can be lowered to facilitate

future implantation using a core biopsy needle, similar to gold-seed fiducial implants used to mark tumors for radiotherapy [33]. Future work in minimizing the size enables harnessing a network of such implants for 3D reconstruction of the tumor microenvironment (TME) as analyzed in [34]. Reducing the eventual form factor will enable implantation through minimally invasive procedures (such as a biopsy), opening the door to continual *in vivo* monitoring at the cellular scale.

The thesis is organized into the following chapters. Chapter 1 is the introduction. In chapter 2, fluorescence microscopy is introduced and the requirements and challenges of *in vivo* fluorescence microscopy for Immunotherapy are outlined to derive the design specifications of the proposed system.

Chapter 3 provides specific details regarding the imager array and wireless interface. The properties of the imager array are subsequently utilized to establish the requirements of the wireless link using a piezoceramic transducer.

Chapter 4 describes the design process of the system and the circuit-level architecture of main blocks. Each block is characterized separately to confirm functionality. The performance of the main blocks and device characterization details are included in this chapter.

Chapter 5 details the benchtop experimental setup for wireless mode fluorescence microscopy including sample preparation and chip fabrication with the optical components. The experimental results validating the wireless system's overall performance for the setup reported in the are presented in here.

The conclusion and comparison with the state-of-the-art are provided in chapter 7. Additionally, future directions and steps to facilitate *in vivo* fluorescence microscopy are included.

Chapter 2

Fluorescence Microscopy

To design a system for wireless fluorescence microscopy integrating the imager array and optical source at the system level is critical since external light sources cannot penetrate deep into the tissue more than a few millimeters. To determine the imager specifications and the necessary optical power from the light source, it is crucial to quantify the fluorescence signal from microscopic cell foci in Immunotherapy. In this chapter, the method for quantifying the fluorescence signal utilizing biological samples from an Immunotherapy experiment is explained and the optical requirements of the light source are derived.
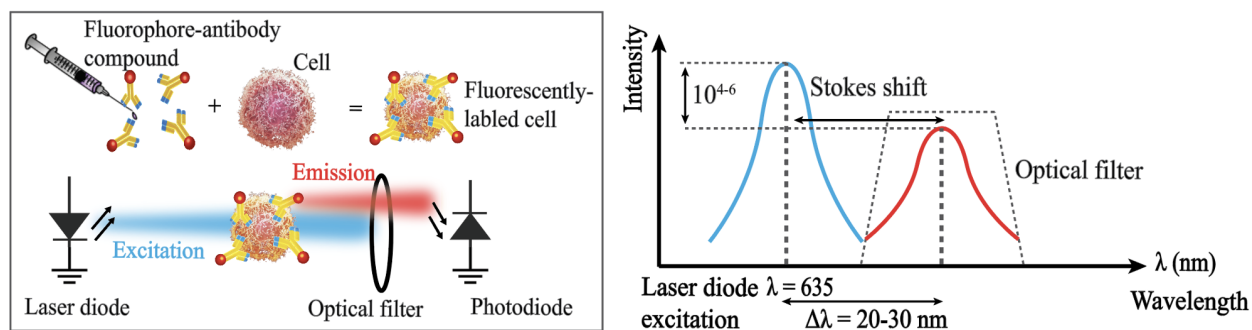
Figure 2.1: Fluorescence microscopy for fluorescently labeled targets using a laser diode, an optical filter and a photodiode.

Fluorescence is a phenomena that involves absorbance and emission of light by a fluorescent molecule referred to as a fluorophore. It occurs when an electron that is excited to a higher and more unstable energy state relaxes to its ground state by emitting photons. Fluorescence microscopy starts with labeling the target cells with fluorophore-labeled antibodies prior to imaging as illustrated in Fig.2.1. For *in vivo* applications, this is typically accomplished through IV administration of the antibody-fluorophore conjugate. The fluorophore sets the wavelength for imaging, and the antibody specificity ensures the labeling of the tar-

get cell type. After binding to the target cells, the fluorophores emit photons with a longer wavelength (shown in red) than the excitation light (shown in blue) after a small Stokes shift in wavelength ($< 50nm$). The excitation and emission lights are shown in Fig.2.1. Due to the inefficiency of the fluorophores in emitting light, higher excitation intensities up to 6 orders of magnitude are required. Therefore, a high pass or bandpass optical filter is necessary to reduce the excitation light's intensity and avoid saturating the photodiodes on the sensor. The commonly used organic fluorescent dyes in biomedical research (such as Cy5 and IRDye800cw) feature Stokes shifts of only $20 - 30nm$ [35], [36], necessitating high-Q optical filters with high out-of-band attenuation ($> 60dB$) to eliminate bleed-through from the higher-intensity excitation to the emission band.

2.1 Signal Quantification

The fluorescence signal strength of fluorophores bound to cell foci can be estimated by taking into account the excitation power of the optical source, the optical properties of the fluorophores (quantum yield and absorption cross-section), and the number of fluorophores per cell. The fluorescence signal for a cluster of cells is given by

$$F = \sigma Q P_{in} N_{fl} N_{cell} \tag{2.1}$$

where F represents the fluorescence signal, σ is the absorption cross-section of the fluorophores in cm^2, Q is the fluorescence quantum yield, P_{in} is the incident optical intensity in mW/cm^2, N_{fl} is the number of fluorophores attached to the target cell, and N_{cell} is the total number of cells in the cluster. Typical antibodies demonstrate an average binding of 10^6 per cell [37], with 1-5 fluorophores per antibody, resulting in $\sim 10^6$ fluorophores per cell [38], Typically fluorophores have a quantum yield of 20%, and an average absorption cross-section on the order of $10^{-16} cm^2$ [39], [40]. To evaluate the immune system's response, changes in the number and position of cells are critical. For example, to detect the fluorescence signal from a cluster of 500 cells with SNR¿10 dB, using an image sensor designed with the photodiodes in [32], a high $> 50mW/cm^2$ optical excitation intensity is required.

To derive the specifications for fluorescence microscopy for Immunotherapy applications, in an experiment Immunotherapy is delivered to mice implanted with tumors, we analyzed fluorescence images from sectioned lymph nodes of an untreated and treated mouse with a functional immune system (BL6 mice) against cancer (colorectal cancer, MC38 cell line). The number of CD8 T-cells, a principal component of the immune system's response to cancer, was estimated by staining the lymph node slides with antibodies targeting CD8 T-cells and counting them. The $1.3mm^2$ cross-sectional samples in Fig.2.2 indicate an increase of $\sim 500 - 1000$ in the number of CD8 T-cells (Cy5 channel, shown in pink and overlaid with the cell nuclei of the entire sample shown in blue) proliferating the lymph node of a responder mouse, which is consistent with the estimated value for N_{cell} in equation 2.1. Increasing populations of CD8 T-cells shown in fluorescence images of the TME is also

supported by current studies in Immunotherapy as an indicator of the immune response [41], [42].
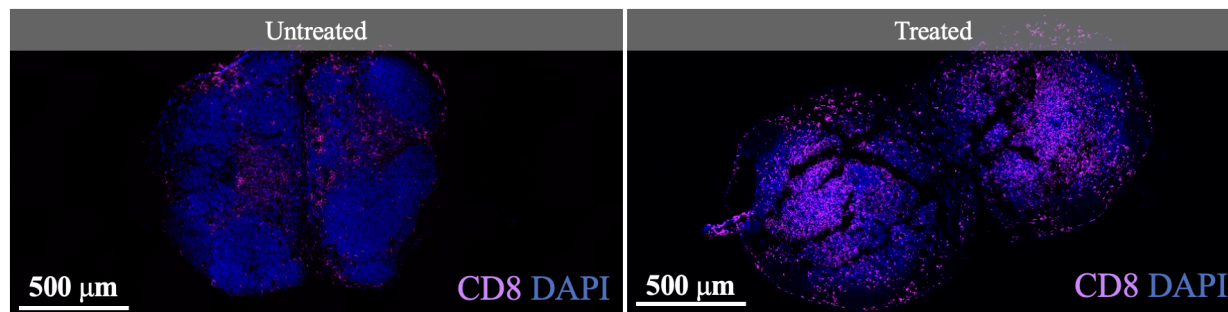
Figure 2.2: Fluorescence images of CD8 T-cells in the lymph nodes of an untreated and treated mouse after Immunotherapy.

2.2 Optical Power Requirements

In addition to the emitted photons, the scattered excitation light from the background contributes to the photodiode signal. Given the typical $20 - 30nm$ Stokes shift of the common organic fluorophores and the high excitation intensity ($\sim 50mW/cm^2$), even using a filter with high out-of-band attenuation of up to $60dB$ can result in bleed-through of the excitation light and saturation of the pixels. To avoid background light leakage from the excitation source through the filter, a laser diode which typically has an FWHM of less than $2nm$ is chosen over an LED with a longer FWHM of about $100nm$.

The electro-optical PIV characterization of the LD (CHIP-635-P5, Roithner LaserTechnik) with a peak excitation wavelength of $635nm$ using a power meter (PM100D, Thorlabs) is shown in 2.3. The forward voltage is shown on the left axis. The optical power and overall efficiency of the diode are shown on the right. The nominal forward voltage and current of $2.1V$ and $37mA$, respectively, result in a total measured optical power of $3.4mW$ and an electrical to optical efficiency of 4.4%, driving the need for significant power delivery to the sensor for fluorescence imaging. Details of integrating the LD in the system and supplying it while imaging the samples are included in chapter 3.
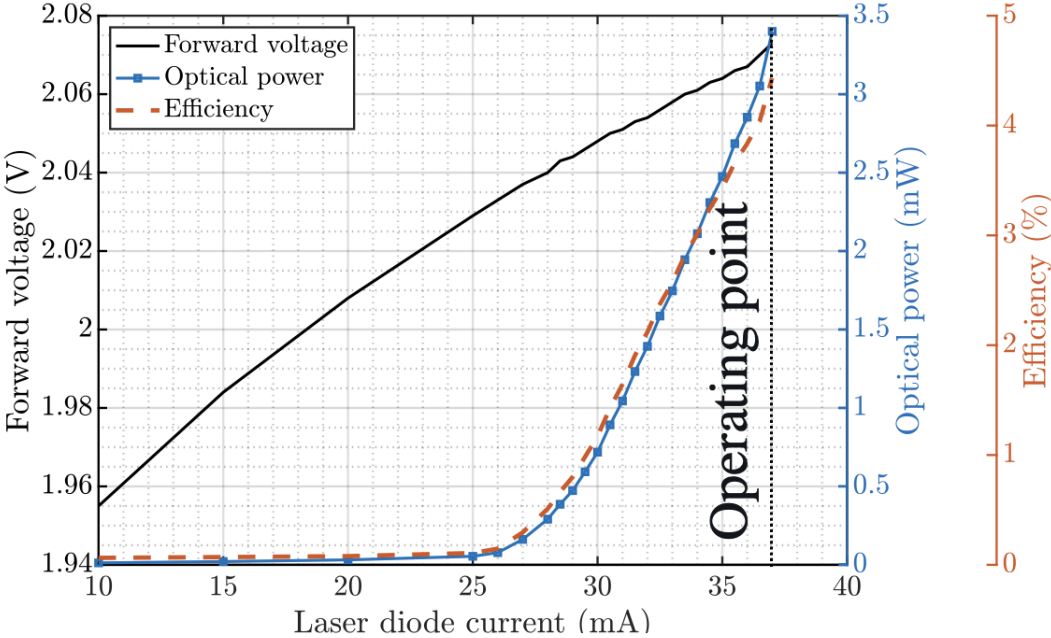
Figure 2.3: PIV characterization of the sub-mm-sized laser diode

Chapter 3

Wireless Fluorescence Microscope

The proposed wireless image sensor shown in Fig.3.1 [43] consists of 1) a 36×40-pixel lensless CMOS image sensor 2) a sub-mm-sized laser diode, 3) a single $1.5\times1.5\times1.5mm^3$ piezoceramic (Lead Zirconate Titanate, PZT) transceiver and 4) an off-chip storage capacitor. Supplying the high $78mW$ instantaneous power to the LD, measured in chapter 2, with the available power of acoustic waves necessitates duty-cycled operation. Thus, the Charge-Up state (when the required energy for taking an image is stored) is separated from the Imaging state (when the stored energy is used to illuminate the sample and capture the image) in the time domain. This section outlines the system-level requirements of integrating the imager array and acoustic interface for chip-scale fluorescence microscopy.

3.1 Pixel Array

The design of the imager array is based on our previous work in [32]. Each pixel incorporates a $44 \times 44\mu m^2$ photodiode and has a pitch of $55\mu m$. The pixels are fabricated in a $0.18\mu m$ 1.8/5/32 V TSMC CMOS process with a dark current density of $14aA/\mu m^2$ and a responsivity equal to $0.11A/W$. To eliminate bulky optical lenses, on-chip microfabricated structures based on angle-selective gratings (ASGs) are utilized to restrict the angle of incident light resulting in images with higher spatial resolution [32]. The use of ASG, along with in-pixel electronics, yields a fill factor of 28% for the imager array.

Imaging is performed using a global shutter as the LD only illuminates the sample for a limited time, which is by far the primary power-consuming operation of the imager, and therefore all pixels must image during this limited time window. This demands that each pixel be able to amplify, sample and hold its data until it is read out via a single channel US-based uplink. Each pixel consists of a capacitive trans-impedance amplifier (CTIA) with a custom-designed integration capacitor $C_{int} = 11fF$. The photodiode signal of each pixel can be computed from

$$V_{signal} = i_{pd}T_{int}/C_{int} \tag{3.1}$$

where i_{pd} is the photodiode current and T_{int} is the integration time [32].
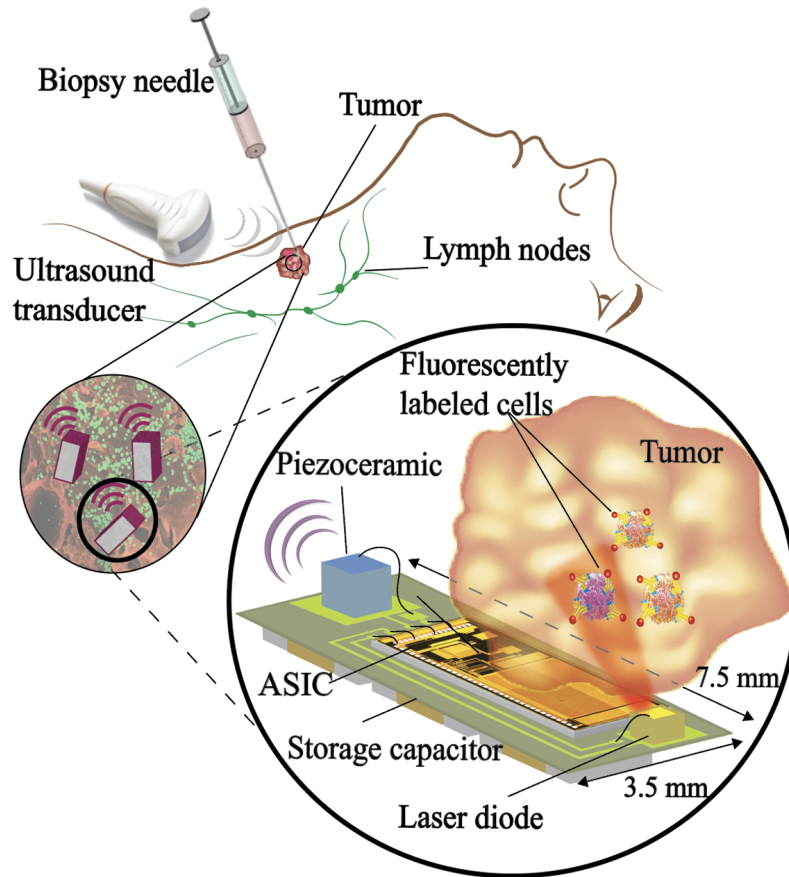
Figure 3.1: Conceptual system diagram of the wireless imaging system in the tumor microenvironment.

The pixel size is chosen to maximize sensitivity to the dynamics of small cell foci (a few 100 cells) for evaluating the Immunotherapy response as discussed in chapter 2. To capture cell movements in real-time, the pixel must be small enough to track the displacement of cells within consecutive frames. The minimum interval between frames is constrained by the charging time of the storage capacitor as it is used to supply the energy for the LD's operation during the Imaging state. Therefore, given a constant power consumption of the LD, the minimum frame time is a function of the time it is switched on, T_{int}. For each value of T_{int}, the pixel dimension must be consistent with the typical displacement of cells with an average velocity of $10 - 20 \mu m/min$ ([44],[45]) between each frame. Pixels with dimensions much larger than this displacement may miss the changes in the cell proliferation profile. Conversely, designing an imager array with the same imaging area using smaller pixels results in unnecessarily oversampling the scene. As discussed in [37] there is a fundamental trade-off for the size of a pixel between maximizing the signal and maintaining spatial resolution. The

received fluorescence signal is proportional to the active area of the photodiodes until the field of view of a pixel matches the size of the foci being imaged. It should be noted that the goal is to track changes in cellular distribution (in response to therapy), and not to obtain intracellular or single-cell imaging. Thus, too small of a pixel will capture noise with only a minimal detected signal which results in a low SNR. The typical $\sim 10\mu m$ dimension of each cell introduces a lower bound for the pixel size. Given the size of the pixel's peripheral circuitry needed to ensure in-pixel low noise amplification and sample and hold for a global shutter system, shrinking the pixel size lowers both the fill factor and the sensitivity to light. Subtending a $5mm^2$ field of view inside the tumor microenvironment which encompasses approximately 500 CD8 T-cells, a key driver of immune response, (at $\sim 100\mu m^2/cell$ and a sparse 1% CD8 T-cell proliferation ratio) with smaller pixels results in larger arrays with higher power consumption and longer readout times. The spatial resolution also depends both on the resolution of the angle-selective structures as well as the pixel dimension, and therefore lowering the pixel size significantly beyond the optical resolution will not result in further improvements in resolution. Conversely, larger pixels that reduce spatial resolution collect more dark current in addition to the photodiode signal, both as a linear function of the area. Given that dark current in this technology is the dominant factor restricting the dynamic range of the pixel, larger pixel area results in increasing the photodiode shot noise which limits the SNR and thereby the minimum detectable signal and sensitivity.

3.2   Wireless Link

The operation of the SoC is divided into multiple states. Imaging only takes place when there is enough charge stored in the off-chip storage capacitor, C_{store}, to power the LD for the entire Imaging state with T_{int} integration time. To minimize average power consumption, various blocks, including the LD driver and the pixel array are power gated and only turned on during their operating states. The simplified model in 3.2 can be used to derive requirements for C_{store} and the wireless link. During imaging, the current of the LD dominates the current consumption of the rest of the chip modeled with R_L. The maximum harvested voltage (V_{rect}) is set to be $5V$ since $5V$ devices are available in the CMOS process. The maximum voltage drop on the storage capacitor during imaging is limited to $1.5V$ to ensure a minimum supply voltage for chip operation after the Imaging state for data conversion and transmission. To achieve the required $37mA$ nominal current for the LD during a $32ms$ integration time, required to capture a $\sim 500 - 1000$ cell foci, C_{store} is chosen to be $0.8mF$. The value of C_{store} can be reduced by using optical sources with higher efficiencies or by allowing a larger voltage drop during imaging. More importantly, 3D tissue samples of a specimen that contain more cells as compared to a single layer of cells on a thin slide (which we are basing our calculations on) inherently produce a larger signal that can be captured with shorter integration times thereby smaller values for C_{store}. Thus, the specifications put forward in this work represent a conservative estimate of the *in vivo* imaging needs, which will likely have a greater number of cells, due to the inherent 3D nature of the tissue (i.e. light penetrates up to several

millimeters, which includes 200-1000 layers of typical $4\mu m$ tissue slices).
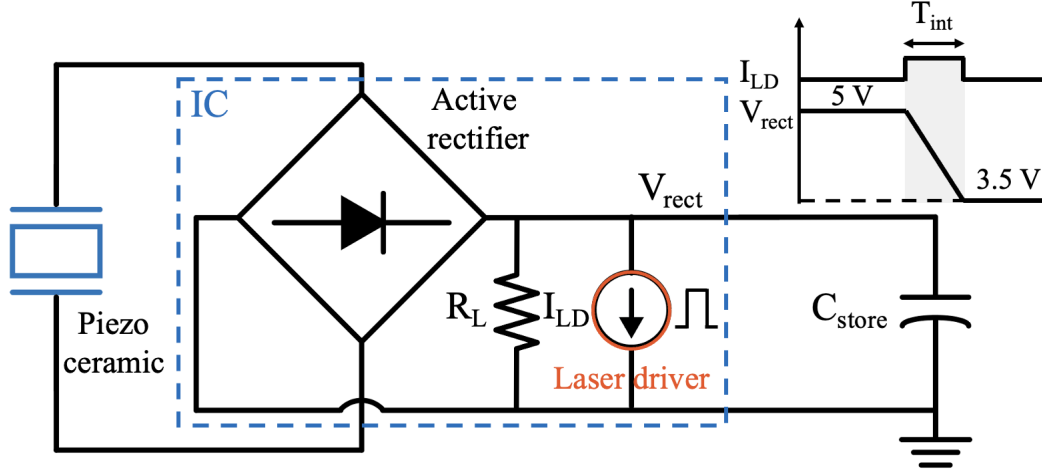
Figure 3.2: Simplified block diagram of the system during the Imaging state. Maximum allowed linear voltage drop on V_{rect} while supplying the laser driver using the charge stored in C_{store}.

To achieve optimal cell movement capture in the TME at a pixel size of $55\mu m$, the sensor frame time must be under a few minutes as the cells move at a rate of approximately $10 - 20\mu m/min$. To charge C_{store} using energy from acoustic waves, a piezoceramic with dimensions of $1.5 \times 1.5 \times 1.5 mm^3$ is selected. In 3.3, the impedance and harvested open circuit voltage of the piezoceramic are characterized against frequency in canola oil with acoustic properties that replicate tissue, featuring an attenuation of around $0.25 dB/cm/MHz$. The frequency dependence of the harvested voltage for the piezoceramic is shown without loading and loaded with the chip's equivalent model. The open circuit voltage is measured with an Olympus acoustic transducer (V303-SU-F0.80IN-PTF). To maintain chip operation, V_{rect} must not drop below $3.5V$, so the maximum peak harvested voltage on V_{rect} is increased to reduce the size of C_{store} for the same acoustic intensity. To achieve the maximum rectified voltage, the operating frequency is tuned to $960kHz$, which is between the series and parallel resonance frequencies of the piezoceramic and the US transducer.
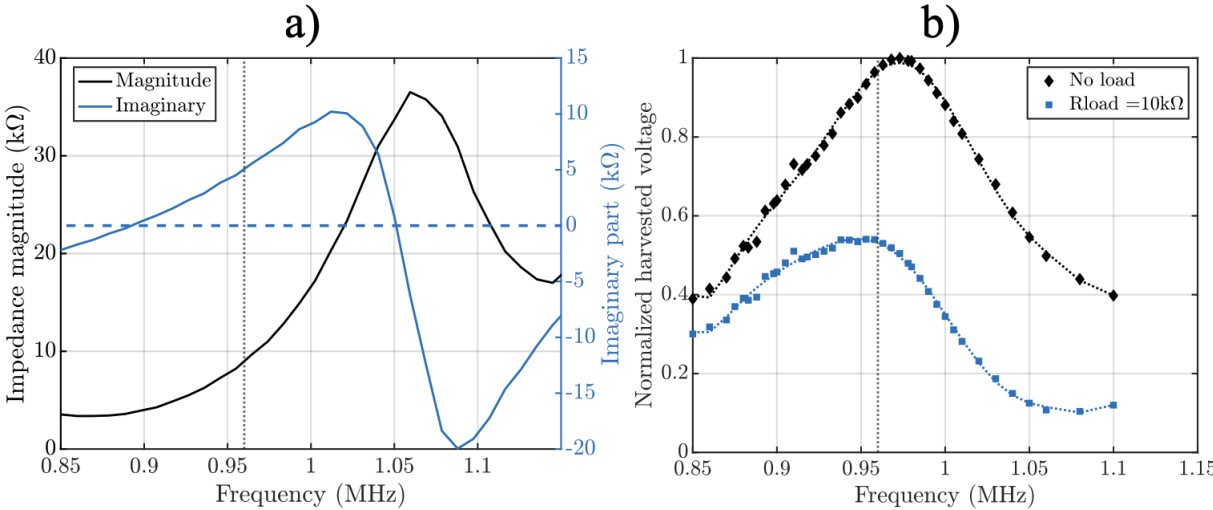
Figure 3.3: Characterization of the $1.5 \times 1.5 \times 1.5mm^3$ piezoceramic: Frequency spectrum of (a) magnitude and imaginary part of the impedance and (b) harvested voltage of the piezoceramic with no load vs. being loaded with the equivalent of the chip's input impedance.

Chapter 4

System design and implementation

The block diagram of the wireless system is shown in Fig.4.1a. The ASIC block diagram displays four primary components: 1) the power management unit (PMU), 2) the imaging front-end, 3) the laser driver, and 4) the Finite State Machine (FSM). The PMU integrates an active rectifier for efficient AC-DC conversion and multiple low-dropout voltage regulators (LDOs) to power various subblocks. Fig.4.1b showcases the imager array in the imaging front-end, with Fig.4.1c presenting the pixel architecture and sample and hold mechanism. The readout circuitry and differential SAR ADC with a unity-gain buffer for pixel data conversion follow the imager array, as illustrated in Fig.4.1a. The laser driver uses the charge from C_{store} to supply the LD, and the FSM governs the state transitions and synchronizes the chip with the external US transducer.

When the emitted US pulses from the external transducer reach the piezoceramic, the active rectifier converts the signal to a dc voltage (V_{rect}) and charges C_{store} up to $5V$. To ensure that the LDO voltages are established, a power-on reset (POR) signal is activated when V_{rect} reaches $4.2V$, initializing the chip and resetting the FSM. On-chip LDOs (1 V, 1.8 V, 2.1 V, 2.5 V, 3.3 V) regulate the supply voltage for the analog front-end, the laser driver, and the FSM. Despite V_{rect}'s significant drop during the Imaging state, the LDOs can function with input voltage values as low as $3.5V$ to ensure the device's digital conversion and backscattering functionality. The CLK signal with a frequency of $960kHz$ is directly extracted from the piezoceramic terminals. The sensor's micrograph is displayed in Fig.4.2, measuring $2.4mm$ by $4.7mm$, with the pixel array accounting for 41% of the overall area. The design and operation of each block are described in detail below.

4.1 Digital Control

Figure.4.3 illustrates the timing diagram and state transitions of the chip. The chip's operation is categorized into 4 states: Charge-Up, Imaging, ADC Operation, and Backscatter Modulation. To simplify data downlink and ensure that on-chip state transitions are synchronized with the external transducer, the projected acoustic carrier is modulated with a
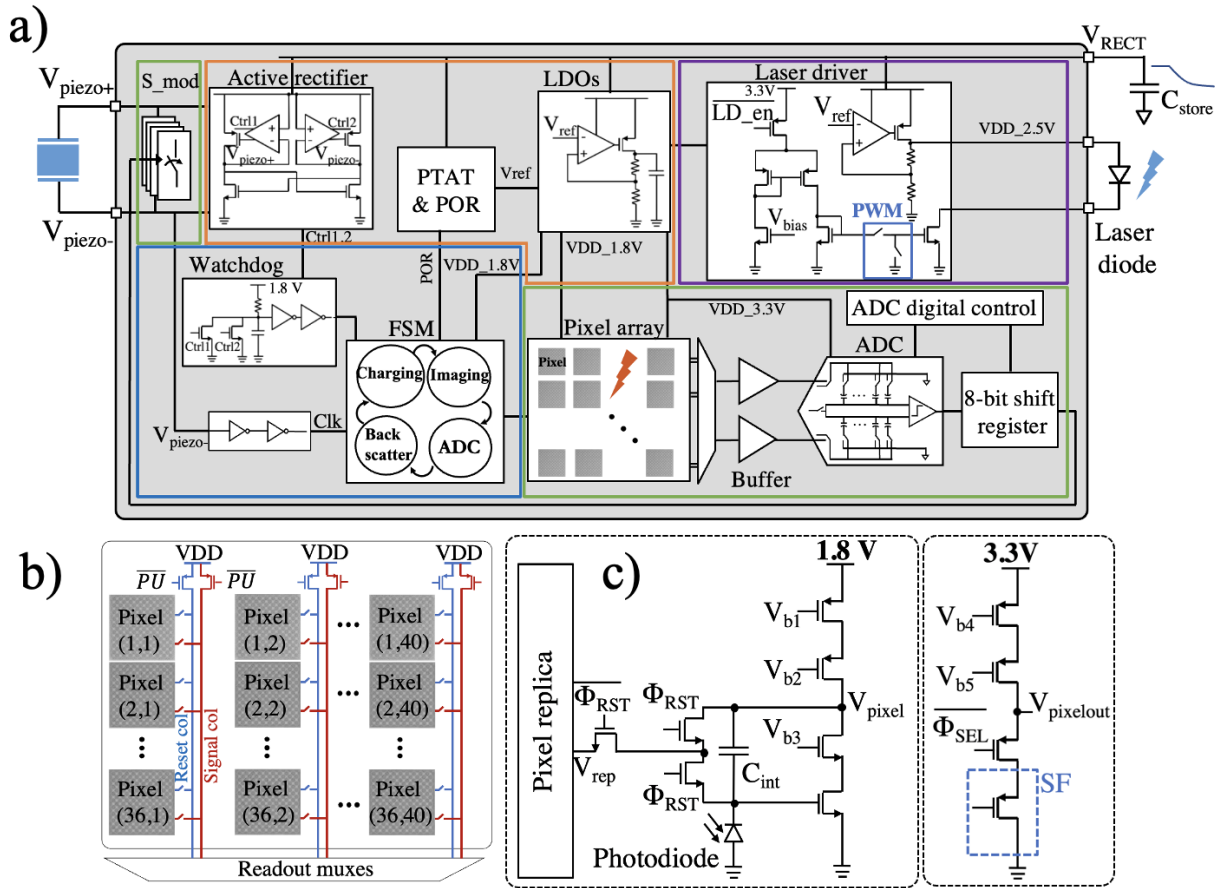
Figure 4.1: (a) Block diagram of the chip including 4 main blocks: power management, imaging front end, laser driver and FSM. The chip is connected to the piezoceramic, external C_{store} and laser diode. (b) The architecture of the imager array with the shared reset and signal lines per column and connected to readout circuitry (c) Schematic of a pixel including the pixel amplifier and the replica circuit to drain the charge stored on C_{int} as discussed in [32] and (d) Sample and hold for correlated double sampling (CDS).

pulse sequence. The different pulse widths of the US signal designated for each state of operation can be easily programmed in an FPGA, which controls the driver of the US transducer, as shown in Fig.4.3 (Vpiezo+). An on-chip watchdog control signal demodulates the incoming US waveform's envelope to navigate the FSM.
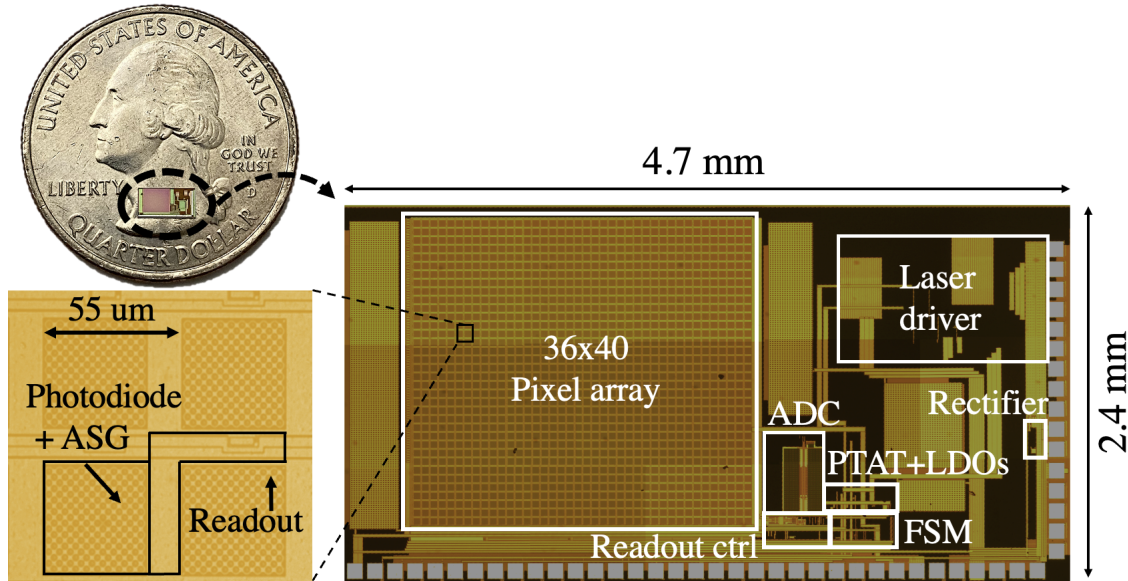
Figure 4.2: Chip micrograph showing the imager array, readout digital control, ADC, rectifier, PTAT, voltage regulators, FSM and laser driver. The chip is $2.4mm$ by $4.7mm$ and the pixel array measures $2mm$ by $2.2mm$. The close-up view shows the pixel with a $55\mu m$ pitch including a $44\mu m$ by $44\mu m$ photodiode area covered with ASGs and the readout circuitry.

4.2   Power Management

To prevent disruption and prolonging the chip's power-up, power-intensive blocks such as the LD driver, pixel array, ADC, and ADC buffers are turned off during Charge-Up. The first falling edge of the watchdog signal during the Imaging state marks the end of the Charge-Up period. The duration of the Charge-Up state can be determined empirically by characterizing the rise time of V_{rect} to reach its final value (5 V) for a given C_{store}. During Imaging, the LD powered sensor illuminates the sample, and after the image is captured, the pixels are read out, digitized, and backscattered sequentially. When not in use during data uplink, the ADC buffers, pixel array, and LD driver are turned off. The voltage of each pixel is digitized and transmitted wirelessly by modulating the impedance of the same piezoceramic used for power transfer. Data transmission continues until the watchdog timer counts all 1440 pixels based on the transitions of the watchdog signal. The data transfer protocol is explained in the next section.
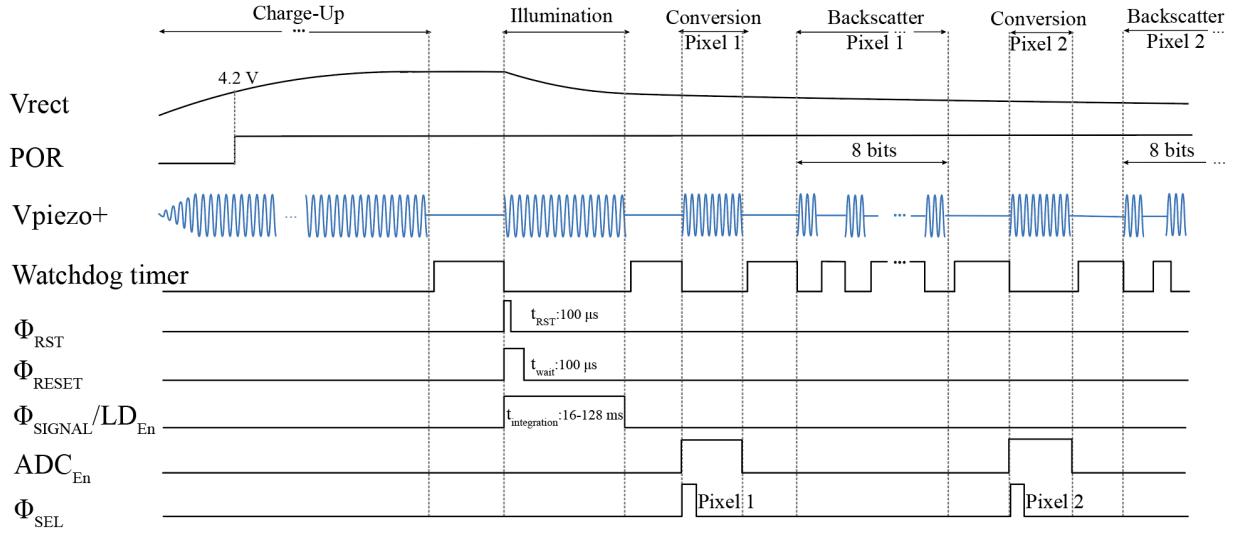
Figure 4.3: Timing diagram and state transitions of the system based on the pattern of the ultrasound waveform received by the piezoceramic (Vpiezo+). The timing control signals for each pixel's operation (Φ_{RST},Φ_{RESET}, Φ_{SIGNAL}) are shown. LD_{En} and ADC_{En} refer to the control signals to turn on the laser driver and ADC, respectively. Φ_{SEL} indicates the sampling phase of the ADC when the pixel's dual outputs (VRES and VSIG) are being read.

4.3 Imaging and Illumination

The chip's operation transitions from Charge-Up to Imaging state, as indicated by the first rising edge of the watchdog pulse, as shown in Fig.4.3. During the Imaging state, the laser driver is enabled, and the pixel array captures the image. The photodiode current generated from the emitted light is integrated into the feedback capacitor of the pixel CTIAs, C_{int}, as illustrated in 4.1c. The output voltage is sampled twice at the beginning and end of the integration time, generating reference and signal values, respectively. This approach, known as correlated double sampling (CDS) helps suppress offset and low-frequency noise of the pixel. A previous work [32] presents a detailed design of the pixels. The laser driver schematic is shown in Fig.4.1a [46]. To prevent overheating of the LD, the driver supplies 50% duty-cycled $50kHz$ current pulses to the laser diode, instead of a continuous current. Thus, the integration time is effectively half the duration of the Imaging state ($T_{int} = 32ms$ for a $64ms$ Imaging state). A PWM controller sets the frequency and duty cycle of the pulses based on the main CLK frequency. The output of the PWM block drives a complementary set of switches to control the current of the driver. The supply voltage of the laser driver is regulated to 2.5 V, complying with the maximum voltage allowed for the LD. An off-chip resistor in series with the LD can adjust the voltage in case of variations. After the Imaging state, the laser driver and pixel array are both turned off. The chip can be configured with

8 different integration times ranging from 8 ms to $64ms$ in steps of 8 ms based on the signal intensity and size of C_{store}.

4.4 Data Communication

After the image is captured, the chip transitions to the ADC Operation and Backscatter Modulation states, as directed by the FSM. During each conversion state, the appropriate row is chosen using digital row-driving circuitry. The signal and reference voltages of each pixel in a row are then sequentially read and sampled during a $5\mu s$ sampling phase using a differential 8-bit SAR ADC. This sampling phase, referred to as Φ_{SEL} in Fig.4.3, turns on the ADC input buffers and selects the correct pixel from the imager array. The output of the ADC is serialized with an 8-bit shift register and is backscattered using pulsed-echo on-off keying (OOK) modulation to maintain a low BER. The 8-bit packet of each pixel is divided into 4 sets of 2 bits that fit within the 26.7 us roundtrip of the acoustic waves in canola oil. The US transducer interrogates the piezoceramic with the modulated waveform and stops for 2ToF after each sequence of 2 bits to eliminate interference from the high voltage power waveform with the weaker backscattered signals. After a single ToF, the signal is modulated based on the acoustic reflection coefficient resulting from the impedance of the chip, R_{Load}. At the series (fs) and parallel (fp) resonance frequencies, the normalized backscattered echo amplitude is proportional to $R_{Load}/(R_{Load} + R_{Lpiezo,s})$ and $R_{piezo,p}/(R_{Load} + R_{piezo,p})$, respectively. For the rest of the frequencies, the reflection coefficient can be computed given the piezoceramic properties and RLoad as quantified in [47]. The modulation switch, S_{Mod} in Fig.4.3, modulates R_{Load} and the echo amplitude for OOK modulation. A programmable switch with 4 impedance values (1,2,4,8 $k\Omega$) sets the modulation depth based on the equivalent impedance of the piezoceramic at the frequency of operation. After the second ToF, the backscattered signal is received on the transducer which is now in the receiving mode. The FSM alternates between ADC and Backscattering states for each pixel until all image data for a single frame is transferred.

4.5 Block-level Characterization

The state transitions of the chip are illustrated in Fig.4.4, following a $150s$ Charge-Up state with a duty cycle of 40% to prevent overheating of the US transducer, the chip moves to the Imaging state, which lasts for $64ms$ and includes a $32ms$ exposure time (T_{int}), as well as a portion of the ADC and Backscatter Modulation states. During the Imaging state, the voltage drops linearly by 1 V, but V_{rect} maintains a voltage greater than $3.5V$ in the subsequent states. The right panel of Fig.4.4 depicts the ADC and Backscattering states for a single pixel, along with the modulated piezoceramic signal that corresponds to the bit values.
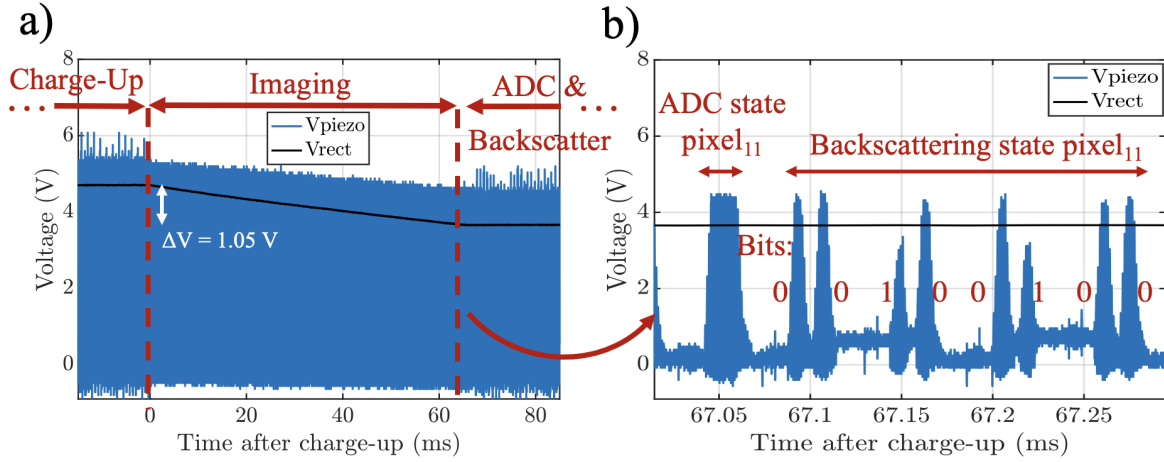
Figure 4.4: (a) State transition diagram including the end of the Charge-Up interval, Imaging state and parts of the ADC and Backscatter Modulation states. Vrect drops linearly during the 64 ms Imaging state with an effective 32 ms integration time (Tint). (b) Detailed transient waveform during the ADC and Backscatter Modulation states for individual pixel.

In order to verify the performance of the laser driver during Tint=48 ms, the optical power of the laser diode is measured using an external photodetector located inside the power meter (PM100D, Thorlabs), as shown in Fig.4.5a. The voltage output of the photodetector (Vpd) is directly proportional to the received optical power from the laser diode. The photodetector voltage signal, displayed in Fig.4.5b, is a 50 kHz signal with a 50% duty cycle that mirrors the transitions of the laser diode's current. Using the PIV characterization of the laser diode presented in Figure 4, the laser diode current is estimated to vary from $37mA$ to $29mA$, which corresponds to optical powers of $3.4mW$ to $0.55mW$, respectively. The 22% decrease in current is attributed to the drop in $Vrect$ throughout the Imaging state, which could be improved with a larger storage capacitor. As a result, the laser driver demonstrates an average electrical efficiency of 66%.

The conversion and backscattering for all pixels take $389ms$ for an implantation depth of 2 cm. The received backscattered waveform is filtered by an FIR filter in software to reconstruct the image. For measurements taken at 2 cm of depth inside canola oil with $V_{rect} = 5V$, the modulation depth is 15.3%, resulting in a BER of 8.68×10^{-5}. Lowering V_{rect} to the minimum 3.5 V decreases the modulation depth to 7.4%, increasing the BER to 3.47×10^{-3} for $11.52kbits$, as shown in Fig.4.6.
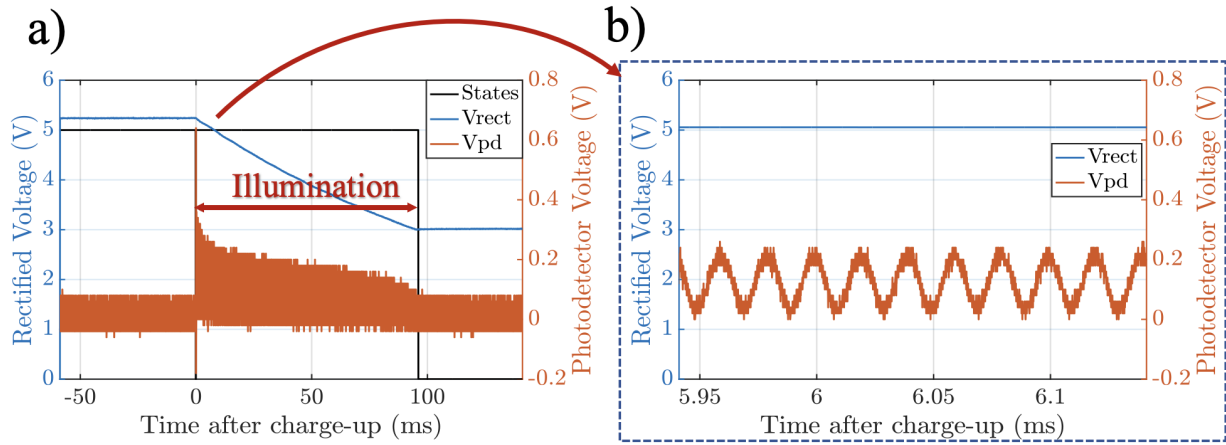
Figure 4.5: Laser driver characterization: (a) Voltage of the embedded photodiode in PM100D power meter during a 96 ms Imaging interval and the linear drop of V_{rect} (b) Close-up showing the 50% duty-cycled, 50 kHz photodetector output voltage indicating the pulsed current of the laser diode supplied by the laser driver. (The measured sinusoidal waveform instead of a pulse signal is due to the limited BW of PM100D).
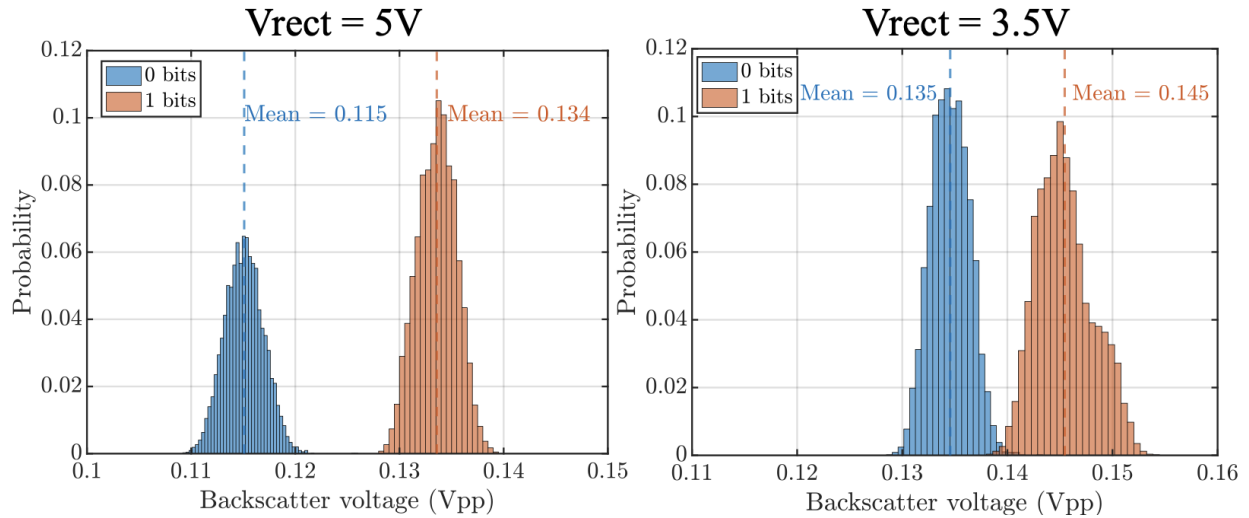
Figure 4.6: Histogram for 0 and 1 bits with a modulation depth of 15.3% and BER of 8.6×10^{-5} for $V_{rect} = 5V$ and modulation depth of 9.7% and BER of 3.47×10^{-3} for $V_{rect} = 3.5V$.

Chapter 5

Experimental Results

5.1   Experimental Setup

Once the individual blocks of the system were tested and their performance was verified, the overall system operation was assessed by imaging a fluorescent dye (Cyanine5.5-NHS) placed underneath a resolution test target (USAF, Thorlabs). During this measurement, the acoustic waves generated by the transducer were used to power up the device and capture an image. Then, the backscattered pixel data was transmitted back to the transducer for image reconstruction processing.

The setup used for the measurement is depicted in Fig.5.1. The piezoceramic is located 2 cm below the US transducer in canola oil. To minimize reflections from the bottom and sides of the tank, an acoustic absorber (Aptflex F28P, Precision Acoustics) is utilized. The transducer is controlled by a high voltage pulser board (Max14808, Maxim Integrated) that is digitally managed by an FPGA to implement the required interrogation sequence to the chip, as shown in Fig.4.3. The piezoceramic is connected to the chip in the optical setup outside, where it is assembled with the optical filter and the fiber optic plate. To evaluate the image resolution, the USAF resolution target, covered with Cyanine5.5-NHS (Excitation: 683 nm, Emission: 703 nm), is positioned on top of the imager array, providing fine spatial features.

5.2   Experimental Results

The images presented in Fig.5.2 were captured from the highlighted regions of the resolution target after a 150 s Charge-Up interval. To prevent the transducer from overheating, the ultrasound interrogation is 40% duty-cycled instead of being continuous. The backscattered data is captured by the transducer after a $T_{int} = 32ms$ and processed using an FIR filter in MATLAB, with a total readout time of $389ms$. The frame time is sufficient to capture movements of cells within the body [44],[45]. Our platform is capable of distinguishing metallic patterns and gaps as small as $140\mu m$, making it suitable for detecting clusters of
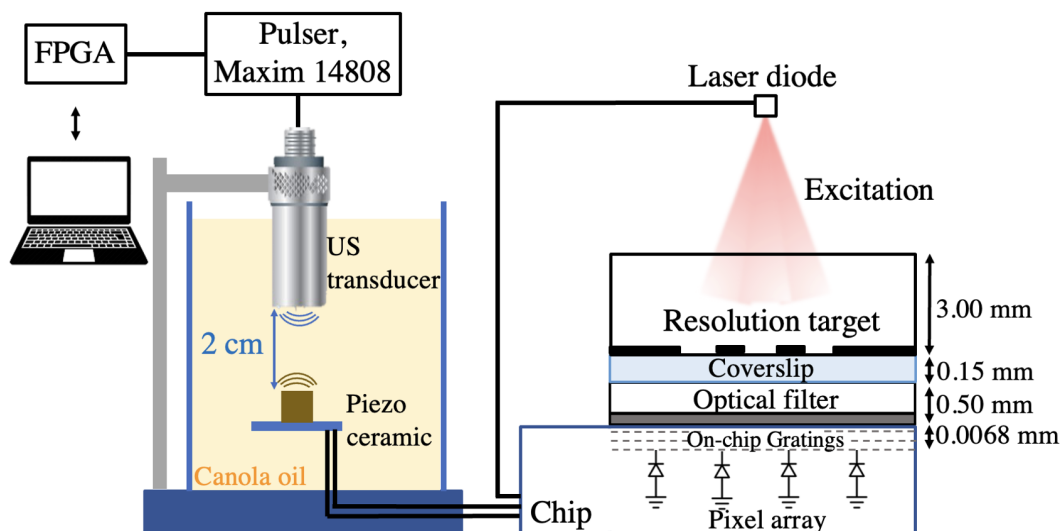
Figure 5.1: Measurement setup for imaging patterns in a USAF resolution target covered with a coverslip containing Cy5.5 fluorescent dye. On the left, the acoustic setup is shown inside a tank of canola oil. The right panel shows the imaging setup which is powered by the piezoceramic.
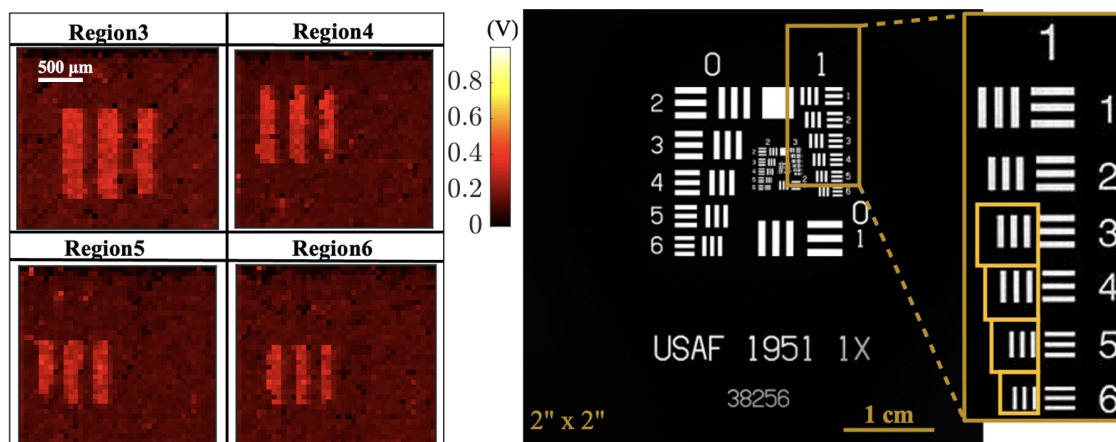
Figure 5.2: Backscattered images from the highlighted regions on the UCSF resolution target. The scale bar is in V. The images are taken with $T_{int} = 32ms$.

a few hundred cells in immunotherapy. The bright pixels in the dark region correspond to the BER while backscattering with the lower V_{rect} values. To further improve image quality, multiple images can be taken and averaged.

Chapter 6

Conclusion

6.1 Summary and Comparison

Table6.1 presents a comparison between our wireless prototype for untethered chip-scale fluorescence microscopy and recently published implantable imagers. The wired implantable imagers in [25], [26], [28] utilize CMOS photodiodes or single photon avalanche diodes (SPADs) for high-resolution fluorescence microscopy. However, their application for continuous in vivo monitoring is limited due to the risk of infection from external wiring. The thermoacoustic sensor in [29] provides a wireless interface for untethered implantation, but it lacks the resolution necessary for multicellular-level detection in biological applications.

Our system represents the first wireless prototype for untethered chip-scale fluorescence microscopy, integrating the optical source to eliminate bulky components such as focusing lenses, fibers, batteries, or external wiring. This proof-of-concept prototype enables real-time microscopy within tissue, addressing a key challenge in assessing therapeutic response and disease progression. The system uses stored wireless energy from an ultrasound link to provide the high instantaneous power ($78mW$) required for the optical source during a $32ms$ integration time. Each frame's $11.52kbits$ of image data are transmitted wirelessly via ultrasound backscattering using the same piezoceramic transceiver for power transfer. The device performance is verified by resolving $140\mu m$ features on a USAF resolution test target and wirelessly transmitting the data via ultrasound backscattering.

6.2 Future Work

The proposed wireless fluorescence image sensor is a proof-of-concept device that offers high-resolution fluorescence microscopy, making it suitable for *in vivo* imaging inside tissue without the need for external wiring. To facilitate its use in minimally invasive implantation using a core biopsy needle, several key steps have been identified, including the following:

The use of a laser diode with higher electrical to optical efficiency, such as the CHIP-650-P5 from Roithner LaserTechnik, which has a 12.5% efficiency, can significantly reduce

	Pollmann et al. , *bioRxiv* 2023 [23]	Zhu et al. , *TBioCAS* 2023 [24]	Kobayashi et al. , *Sci Rep* 2016 [26]	Sawaby et al. , *VLSI* 2018 [27]	**This work**
Imaging method	Fluorescence Lifetime Imaging	Fluorescence	Fluorescence	Thermoacoustic	**Fluorescence**
Multi-cellular resolution	Yes	No	Yes	No	**Yes**
Technology	130 nm HV CMOS	65 nm LP CMOS	350 nm CMOS	65 nm CMOS	**180 nm CMOS**
Wireless Power Transfer	No	No	No	Yes	**Yes**
Wireless Communication	No	Yes	No	Yes	**Yes**
Power source	Power supply	Battery	Power supply	Ultrasound	**Ultrasound**
Array size	192×256	3x5	120 x 268	1 x 16[a]	**36 x 40**
Pixel size	25.3 x 51.2 μm^2	150 x 170 μm^2	7.5 x 7.5 μm^2	--	**55 x 55 μm^2**
Excitation time	2 ns			5 μs	**8-64 ms**
Excitation source	μLED	LED	μLED	RF	**Laser diode**
Fluorophores Stokes shift	gCaMP6f 20-30 nm	Qdot800 400 nm	GFP 30 nm	--	**Cy5, Cy5.5 20-30 nm**
Implant depth	--	--	--	6 cm	**2 cm**
Data transmitted per frame	Digital 3 kbits	Digital 10 bits	Analog	Digital 72[b] kbits	**Digital 11.5 kbits**

[a] Number of CMUT channels   [b] Estimated 144 bits based on 9-bit ADC and 16 channels, 72 kbit based on memory size

Figure 6.1: Comparison Table of Implantable Image Sensors.

the required stored charge in C_{store}, by more than 64%, while maintaining the same optical power. Reducing Tint and averaging two consecutive images, each taken with half of the standard integration time, can maintain the signal-to-noise ratio (SNR) with only a 1dB reduction in value, which can lower the size of C_{store} by 50%.

The scalable design of the CMOS imager sensor allows for various array sizes tailored to the physical requirements of the application. Sensitivity enhancement techniques can also be employed to improve the performance of the device.

Bibliography

[1] H. C. Koydemir and A. Ozcan, "Wearable and implantable sensors for biomedical applications," *Annual Review of Analytical Chemistry*, vol. 11, no. 1, pp. 127–146, Jun. 12, 2018, ISSN: 1936-1327, 1936-1335. DOI: `10.1146/annurev-anchem-061417-125956`. [Online]. Available: `https://www.annualreviews.org/doi/10.1146/annurev-anchem-061417-125956`.

[2] A. Yadegari, M. A. Karami, and M. R. Daliri, "Neural monitoring with CMOS image sensors," *Basic and Clinical Neuroscience*, vol. 9, no. 3, pp. 227–235, 2018, ISSN: 2008-126X. DOI: `10.29252/NIRP.BCN.9.3.227`. [Online]. Available: `https://www.ncbi.nlm.nih.gov/pmc/articles/PMC6037429/`.

[3] A. van Weverwijk and K. E. de Visser, "Mechanisms driving the immunoregulatory function of cancer cells," *Nature Reviews Cancer*, pp. 1–23, Jan. 30, 2023, Publisher: Nature Publishing Group, ISSN: 1474-1768. DOI: `10.1038/s41568-022-00544-4`. [Online]. Available: `https://www.nature.com/articles/s41568-022-00544-4`.

[4] A. D. Waldman, J. M. Fritz, and M. J. Lenardo, "A guide to cancer immunotherapy: From t cell basic science to clinical practice," *Nature Reviews Immunology*, vol. 20, no. 11, pp. 651–668, Nov. 2020, Number: 11 Publisher: Nature Publishing Group, ISSN: 1474-1741. DOI: `10.1038/s41577-020-0306-5`. [Online]. Available: `https://www.nature.com/articles/s41577-020-0306-5`.

[5] J. M. Kirkwood, L. H. Butterfield, A. A. Tarhini, H. Zarour, P. Kalinski, and S. Ferrone, "Immunotherapy of cancer in 2012," *CA: A Cancer Journal for Clinicians*, vol. 62, no. 5, pp. 309–335, 2012, _eprint: https://onlinelibrary.wiley.com/doi/pdf/10.3322/caac.20132, ISSN: 1542-4863. DOI: `10.3322/caac.20132`. [Online]. Available: `https://onlinelibrary.wiley.com/doi/abs/10.3322/caac.20132`.

[6] S. L. Topalian, C. G. Drake, and D. M. Pardoll, "Immune checkpoint blockade: A common denominator approach to cancer therapy," *Cancer Cell*, vol. 27, no. 4, pp. 450–461, Apr. 13, 2015, ISSN: 1535-6108. DOI: `10.1016/j.ccell.2015.03.001`. [Online]. Available: `https://www.sciencedirect.com/science/article/pii/S1535610815000896`.

[7] K. J. Hiam-Galvez, B. M. Allen, and M. H. Spitzer, "Systemic immunity in cancer," *Nature Reviews Cancer*, vol. 21, no. 6, pp. 345–359, Jun. 2021, Number: 6 Publisher: Nature Publishing Group, ISSN: 1474-1768. DOI: `10.1038/s41568-021-00347-z`. [Online]. Available: `https://www.nature.com/articles/s41568-021-00347-z`.

[8] L. B. Kennedy and A. K. S. Salama, "A review of cancer immunotherapy toxic-ity," *CA: A Cancer Journal for Clinicians*, vol. 70, no. 2, pp. 86–104, 2020, _eprint: https://onlinelibrary.wiley.com/doi/pdf/10.3322/caac.21596, ISSN: 1542-4863. DOI: `10.3322/caac.21596`. [Online]. Available: `https://onlinelibrary.wiley.com/doi/abs/10.3322/caac.21596`.

[9] V. Verma, T. Sprave, W. Haque, *et al.*, "A systematic review of the cost and cost-effectiveness studies of immune checkpoint inhibitors," *Journal for Immunotherapy of Cancer*, vol. 6, p. 128, Nov. 23, 2018, ISSN: 2051-1426. DOI: `10.1186/s40425-018-0442-7`. [Online]. Available: `https://www.ncbi.nlm.nih.gov/pmc/articles/PMC6251215/`.

[10] S. Kalaora, A. Nagler, J. A. Wargo, and Y. Samuels, "Mechanisms of immune ac-tivation and regulation: Lessons from melanoma," *Nature Reviews Cancer*, vol. 22, no. 4, pp. 195–207, Apr. 2022, Number: 4 Publisher: Nature Publishing Group, ISSN: 1474-1768. DOI: `10.1038/s41568-022-00442-9`. [Online]. Available: `https://www.nature.com/articles/s41568-022-00442-9`.

[11] A. Sahu, K. Kose, L. Kraehenbuehl, *et al.*, "In vivo tumor immune microenvironment phenotypes correlate with inflammation and vasculature to predict immunotherapy response," *Nature Communications*, vol. 13, no. 1, p. 5312, Sep. 9, 2022, Number: 1 Publisher: Nature Publishing Group, ISSN: 2041-1723. DOI: `10.1038/s41467-022-32738-7`. [Online]. Available: `https://www.nature.com/articles/s41467-022-32738-7`.

[12] F. F. A. Saad, *Molecular Imaging*. IntechOpen, May 15, 2013, Publication Title: Se-lected Topics on Computed Tomography, ISBN: 978-953-51-1102-3. DOI: `10.5772/55907`. [Online]. Available: `https://www.intechopen.com/chapters/44608`.

[13] C. Andreou, R. Weissleder, and M. F. Kircher, "Multiplexed imaging in oncology," *Nature Biomedical Engineering*, vol. 6, no. 5, pp. 527–540, May 2022, Number: 5 Pub-lisher: Nature Publishing Group, ISSN: 2157-846X. DOI: `10.1038/s41551-022-00891-5`. [Online]. Available: `https://www.nature.com/articles/s41551-022-00891-5`.

[14] L. Seymour, J. Bogaerts, A. Perrone, *et al.*, "iRECIST: Guidelines for response criteria for use in trials testing immunotherapeutics," *The Lancet. Oncology*, vol. 18, no. 3, e143–e152, Mar. 2017, ISSN: 1470-2045. DOI: `10.1016/S1470-2045(17)30074-8`. [Online]. Available: `https://www.ncbi.nlm.nih.gov/pmc/articles/PMC5648544/`.

[15] Y. W. Choo, J. Jeong, and K. Jung, "Recent advances in intravital microscopy for in-vestigation of dynamic cellular behavior in vivo," *BMB Reports*, vol. 53, no. 7, pp. 357–366, Jul. 31, 2020, ISSN: 1976-6696. DOI: `10.5483/BMBRep.2020.53.7.069`. [Online]. Available: `https://www.ncbi.nlm.nih.gov/pmc/articles/PMC7396917/`.

[16] "Imaging more of the body," *Nature Biomedical Engineering*, vol. 6, no. 5, pp. 495–496, May 2022, Number: 5 Publisher: Nature Publishing Group, ISSN: 2157-846X. DOI: `10.1038/s41551-022-00897-z`. [Online]. Available: `https://www.nature.com/articles/s41551-022-00897-z`.

[17] C. Li and Q. Wang, "Challenges and opportunities for intravital near-infrared fluorescence imaging technology in the second transparency window," *ACS Nano*, vol. 12, no. 10, pp. 9654–9659, Oct. 23, 2018, ISSN: 1936-0851, 1936-086X. DOI: `10.1021/acsnano.8b07536`. [Online]. Available: `https://pubs.acs.org/doi/10.1021/acsnano.8b07536`.

[18] M. Alieva, L. Ritsma, R. J. Giedt, R. Weissleder, and J. van Rheenen, "Imaging windows for long-term intravital imaging," *IntraVital*, vol. 3, no. 2, e29917, Aug. 11, 2014, ISSN: 2165-9087. DOI: `10.4161/intv.29917`. [Online]. Available: `https://www.ncbi.nlm.nih.gov/pmc/articles/PMC5312719/`.

[19] A. Singer and J. T. Robinson, "Wireless power delivery techniques for miniature implantable bioelectronics," *Advanced Healthcare Materials*, vol. 10, no. 17, p. 2 100 664, 2021, _eprint: https://onlinelibrary.wiley.com/doi/pdf/10.1002/adhm.202100664, ISSN: 2192-2659. DOI: `10.1002/adhm.202100664`. [Online]. Available: `https://onlinelibrary.wiley.com/doi/abs/10.1002/adhm.202100664`.

[20] S. R. Khan, S. K. Pavuluri, G. Cummins, and M. P. Y. Desmulliez, "Wireless power transfer techniques for implantable medical devices: A review," *Sensors (Basel, Switzerland)*, vol. 20, no. 12, p. 3487, Jun. 19, 2020, ISSN: 1424-8220. DOI: `10.3390/s20123487`. [Online]. Available: `https://www.ncbi.nlm.nih.gov/pmc/articles/PMC7349694/`.

[21] D. K. Piech, B. C. Johnson, K. Shen, *et al.*, "A wireless millimetre-scale implantable neural stimulator with ultrasonically powered bidirectional communication," *Nature Biomedical Engineering*, vol. 4, no. 2, pp. 207–222, Feb. 2020, Number: 2 Publisher: Nature Publishing Group, ISSN: 2157-846X. DOI: `10.1038/s41551-020-0518-9`. [Online]. Available: `https://www.nature.com/articles/s41551-020-0518-9`.

[22] S. Sonmezoglu, J. R. Fineman, E. Maltepe, and M. M. Maharbiz, "Monitoring deep-tissue oxygenation with a millimeter-scale ultrasonic implant," *Nature Biotechnology*, vol. 39, no. 7, pp. 855–864, Jul. 2021, Number: 7 Publisher: Nature Publishing Group, ISSN: 1546-1696. DOI: `10.1038/s41587-021-00866-y`. [Online]. Available: `https://www.nature.com/articles/s41587-021-00866-y`.

[23] E. H. Pollmann, H. Yin, I. Uguz, *et al.*, "Subdural CMOS optical probe (SCOPe) for bidirectional neural interfacing," Neuroscience, preprint, Feb. 8, 2023. DOI: `10.1101/2023.02.07.527500`. [Online]. Available: `http://biorxiv.org/lookup/doi/10.1101/2023.02.07.527500`.

[24] C. Zhu, Y. Wen, T. Liu, H. Yang, and K. Sengupta, "An ingestible pill with CMOS fluorescence sensor array, bi-directional wireless interface and packaged optics for in-vivo bio-molecular sensing," *IEEE Transactions on Biomedical Circuits and Systems*, pp. 1–17, 2023, Conference Name: IEEE Transactions on Biomedical Circuits and Systems, ISSN: 1940-9990. DOI: `10.1109/TBCAS.2023.3244570`.

[25] K. Sugie, K. Sasagawa, Y. Ohta, *et al.*, "Implantable CMOS image sensor with a neural amplifier for simultaneous recording of optical and electrophysiological signals," in *2021 IEEE Biomedical Circuits and Systems Conference (BioCAS)*, ISSN: 2163-4025, Oct. 2021, pp. 1–4. DOI: `10.1109/BioCAS49922.2021.9644940`.

[26] T. Kobayashi, M. Haruta, K. Sasagawa, *et al.*, ""optical communication with brain cells by means of an implanted duplex micro-device with optogenetics and ca2+ fluoroimaging"," *Scientific Reports*, vol. 6, no. 1, p. 21 247, Feb. 16, 2016, Number: 1 Publisher: Nature Publishing Group, ISSN: 2045-2322. DOI: `10.1038/srep21247`. [Online]. Available: `https://www.nature.com/articles/srep21247`.

[27] A. Sawaby, M. L. Wang, E. So, *et al.*, "A wireless implantable ultrasound array receiver for thermoacoustic imaging," in *2018 IEEE Symposium on VLSI Circuits*, ISSN: 2158-5601, Jun. 2018, pp. 189–190. DOI: `10.1109/VLSIC.2018.8502293`.

[28] J. Li, H. Ebendorff-Heidepriem, B. C. Gibson, *et al.*, "Perspective: Biomedical sensing and imaging with optical fibers—innovation through convergence of science disciplines," *APL Photonics*, vol. 3, no. 10, p. 100 902, Oct. 2018, Publisher: American Institute of Physics. DOI: `10.1063/1.5040861`. [Online]. Available: `https://aip.scitation.org/doi/10.1063/1.5040861`.

[29] M. M. Ghanbari, D. K. Piech, K. Shen, *et al.*, "A sub-mm3 ultrasonic free-floating implant for multi-mote neural recording," *IEEE Journal of Solid-State Circuits*, vol. 54, no. 11, pp. 3017–3030, Nov. 2019, Conference Name: IEEE Journal of Solid-State Circuits, ISSN: 1558-173X. DOI: `10.1109/JSSC.2019.2936303`.

[30] B. M. G. Rosa and G.-Z. Yang, "Ultrasound powered implants: Design, performance considerations and simulation results," *Scientific Reports*, vol. 10, no. 1, p. 6537, Apr. 16, 2020, Number: 1 Publisher: Nature Publishing Group, ISSN: 2045-2322. DOI: `10.1038/s41598-020-63097-2`. [Online]. Available: `https://www.nature.com/articles/s41598-020-63097-2`.

[31] "Marketing clearance of diagnostic ultrasound systems and transducers - guidance for industry and food and drug administration staff,"

[32] E. P. Papageorgiou, B. E. Boser, and M. Anwar, "Chip-scale angle-selective imager for in vivo microscopic cancer detection," *IEEE Transactions on Biomedical Circuits and Systems*, vol. 14, no. 1, pp. 91–103, Feb. 2020, Conference Name: IEEE Transactions on Biomedical Circuits and Systems, ISSN: 1940-9990. DOI: `10.1109/TBCAS.2019.2959278`.

[33] A. Saad, J. Goldstein, Y. R. Lawrence, *et al.*, "Transperineal implantation of gold fiducial markers (gold seeds) for prostate image-guided radiation therapy: A feasible technique associated with a low risk of complications," *Journal of Medical Radiation Sciences*, vol. 62, no. 4, pp. 261–266, 2015, _eprint: https://onlinelibrary.wiley.com/doi/pdf/10.1002/jmrs, ISSN: 2051-3909. DOI: 10.1002/jmrs.122. [Online]. Available: https://onlinelibrary.wiley.com/doi/abs/10.1002/jmrs.122.

[34] H. Najafiaghdam, R. Rabbani, A. Gharia, E. P. Papageorgiou, and M. Anwar, "3d reconstruction of cellular images from microfabricated imagers using fully-adaptive deep neural networks," *Scientific Reports*, vol. 12, no. 1, p. 7229, May 4, 2022, ISSN: 2045-2322. DOI: 10.1038/s41598-022-10886-6. [Online]. Available: https://www.nature.com/articles/s41598-022-10886-6.

[35] H. Chen, L. Liu, K. Qian, *et al.*, "Bioinspired large stokes shift small molecular dyes for biomedical fluorescence imaging," *Science Advances*, vol. 8, no. 32, eabo3289, Aug. 12, 2022, Publisher: American Association for the Advancement of Science. DOI: 10.1126/sciadv.abo3289. [Online]. Available: https://www.science.org/doi/10.1126/sciadv.abo3289.

[36] U. Resch-Genger, M. Grabolle, S. Cavaliere-Jaricot, R. Nitschke, and T. Nann, "Quantum dots versus organic dyes as fluorescent labels," *Nature Methods*, vol. 5, no. 9, pp. 763–775, Sep. 2008, ISSN: 1548-7091, 1548-7105. DOI: 10.1038/nmeth.1248. [Online]. Available: http://www.nature.com/articles/nmeth.1248.

[37] A. Gharia, E. P. Papageorgiou, S. Giverts, C. Park, and M. Anwar, "Signal to noise ratio as a cross-platform metric for intraoperative fluorescence imaging," *Molecular Imaging*, vol. 19, p. 1 536 012 120 913 693, 2020, ISSN: 1536-0121. DOI: 10.1177/1536012120913693.

[38] K. Sano, M. Mitsunaga, T. Nakajima, P. L. Choyke, and H. Kobayashi, "In vivo breast cancer characterization imaging using two monoclonal antibodies activatably labeled with near infrared fluorophores," *Breast Cancer Research*, vol. 14, no. 2, R61, Apr. 17, 2012, ISSN: 1465-542X. DOI: 10.1186/bcr3167. [Online]. Available: https://doi.org/10.1186/bcr3167.

[39] A. Penzkofer and P. Sperber, "Measurement of absorption cross sections in the long-wavelength region of the s0s1 absorption band of dyes," *Chemical Physics*, vol. 88, no. 2, pp. 309–313, Aug. 1984, ISSN: 03010104. DOI: 10.1016/0301-0104(84)85288-X. [Online]. Available: https://linkinghub.elsevier.com/retrieve/pii/030101048485288X.

[40] E. te Velde, T. Veerman, V. Subramaniam, and T. Ruers, "The use of fluorescent dyes and probes in surgical oncology," *European Journal of Surgical Oncology (EJSO)*, vol. 36, no. 1, pp. 6–15, Jan. 2010, ISSN: 07487983. DOI: 10.1016/j.ejso.2009.10.014. [Online]. Available: https://linkinghub.elsevier.com/retrieve/pii/S0748798309004983.

[41] M. H. Spitzer, Y. Carmi, N. E. Reticker-Flynn, *et al.*, "Systemic immunity is required for effective cancer immunotherapy," *Cell*, vol. 168, no. 3, 487–502.e15, Jan. 2017, ISSN: 00928674. DOI: `10.1016/j.cell.2016.12.022`. [Online]. Available: `https://linkinghub.elsevier.com/retrieve/pii/S009286741631738X`.

[42] C. A. Ferreira, P. Heidari, B. Ataeinia, *et al.*, "Non-invasive detection of immunotherapy-induced adverse events," *Clinical cancer research : an official journal of the American Association for Cancer Research*, vol. 27, no. 19, pp. 5353–5364, Oct. 1, 2021, ISSN: 1078-0432. DOI: `10.1158/1078-0432.CCR-20-4641`. [Online]. Available: `https://www.ncbi.nlm.nih.gov/pmc/articles/PMC8752648/`.

[43] R. Rabbani, H. Najafiaghdam, B. Zhao, *et al.*, "A 36×40 wireless fluorescence image sensor for real-time microscopy in cancer therapy," in *2022 IEEE Custom Integrated Circuits Conference (CICC)*, ISSN: 2152-3630, Apr. 2022, pp. 1–2. DOI: `10.1109/CICC53496.2022.9772779`.

[44] L. Dupré, R. Houmadi, C. Tang, and J. Rey-Barroso, "T lymphocyte migration: An action movie starring the actin and associated actors," *Frontiers in Immunology*, vol. 6, p. 586, Nov. 18, 2015, ISSN: 1664-3224. DOI: `10.3389/fimmu.2015.00586`. [Online]. Available: `https://www.ncbi.nlm.nih.gov/pmc/articles/PMC4649030/`.

[45] M. J. Miller, S. H. Wei, M. D. Cahalan, and I. Parker, "Autonomous t cell trafficking examined in vivo with intravital two-photon microscopy," *Proceedings of the National Academy of Sciences*, vol. 100, no. 5, pp. 2604–2609, Mar. 4, 2003, Publisher: Proceedings of the National Academy of Sciences. DOI: `10.1073/pnas.2628040100`. [Online]. Available: `https://www.pnas.org/doi/10.1073/pnas.2628040100`.

[46] R. Rabbani, H. Najafiaghdam, M. M. Ghanbari, *et al.*, "Towards an implantable fluorescence image sensor for real-time monitoring of immune response in cancer therapy," in *2021 43rd Annual International Conference of the IEEE Engineering in Medicine & Biology Society (EMBC)*, ISSN: 2694-0604, Nov. 2021, pp. 7399–7403. DOI: `10.1109/EMBC46164.2021.9631061`.

[47] M. M. Ghanbari and R. Muller, "Optimizing volumetric efficiency and backscatter communication in biosensing ultrasonic implants," *IEEE Transactions on Biomedical Circuits and Systems*, vol. 14, no. 6, pp. 1381–1392, Dec. 2020, Conference Name: IEEE Transactions on Biomedical Circuits and Systems, ISSN: 1940-9990. DOI: `10.1109/TBCAS.2020.3033488`.